
Quantized Conditional COT-GAN for Video Prediction

Tianlin Xu
Department of Statistics
London School of Economics
t.xu12@lse.ac.uk

Beatrice Acciaio
Department of Mathematics
ETH Zurich
beatrice.acciaio@math.ethz.ch

Abstract

Causal Optimal Transport (COT) results from imposing a temporal causality constraint on classic optimal transport problems, which naturally generates a new concept of distances between distributions on path spaces. The first application of the COT theory for sequential learning was given in Xu et al. [50], where COT-GAN was introduced as an adversarial algorithm to train implicit generative models optimized for producing sequential data. Relying on [50], the contribution of the present paper is twofold. First, we develop a conditional version of COT-GAN suitable for sequence prediction. This means that the dataset is now used in order to learn how a sequence will evolve given the observation of its past evolution. Second, we improve on the convergence results by working with modifications of the empirical measures via a specific type of quantization due to Backhoff et al. [8]. The resulting *quantized conditional COT-GAN* algorithm is illustrated with an application for video prediction.

1 Introduction

Time series prediction is a challenging task. Given past observations, a desirable model should not only capture the distribution of features at each time step, but also predict its complex evolution over time. Autoregressive models which predict one time step after another seem to be a natural choice for learning such a task, see e.g. [16, 27, 33, 49]. However, the drawbacks of autoregressive models are the compounding error due to multi-step sampling and their high computational cost, see e.g. [27, 38]. Most existing models for time series prediction tend to ignore the temporal dependencies in sequences in the loss function, merely relying on certain specific network architectures, such as recurrent neural network (RNN) and 1D and 3D convolutional neural network (CNN), to capture the underlying dynamics, see e.g. [42, 4, 39, 47, 43]. For this learning task, the loss function used to compare prediction and real evolution plays a crucial role. However, a loss function that is blind to the sequential nature of data will almost certainly disappoint.

Yoon et al. [52] proposed TimeGAN to tackle this problem by introducing an auxiliary step-wise loss function to the original GAN objective, which indeed leads to more coherent and accurate predictions. More recently, the advances in the field of causal optimal transport (COT) have shown a promising direction for sequential modeling, see e.g. [7, 8, 35, 50]. This type of transport constrains the transport plans to respect temporal causality, in that the arrival sequence at any time t depends on the starting sequence only up to time t . In this way, at every time we only use information available up to that time, which is a natural request in sequential learning. This is the foundation of COT-GAN [50], where the training objective is tailored to sequential data. This proved to be an efficient tool, leading to generation of high-quality video sequences. Although the sharpness of single frames remains a challenge in video modeling, COT-GAN demonstrates that the evolution of motions can be reproduced in a smooth manner without further regularization.

While COT-GAN is trained to produce sequences, the algorithm we propose here is learning *conditional sequences*, that is, how a sequence is likely to evolve given the observation of its past evolution. For this task, we employ a modification of the empirical measure that was introduced by Backhoff et al. [8] in the framework of *adapted Wasserstein (AW) distance*. AW-distance is the result of an optimal transport problem where the plans are constrained to be causal in both direction (so-called *bicausal optimal transport*); see [35, 36]. This turns out to be the appropriate distance to measure how much two processes differ, when we want to give importance to the evolution of information, see e.g. [9]. As noted in [36] and [8], the AW-distance between a distribution and the empirical measure of a sample from it may not vanish while the size of the sample goes to infinity. To correct for this, Pflug and Pichler [36] proposed a convoluted empirical measure with a scaled smoothing kernel, while Backhoff et al. [8] suggested an adapted empirical measure obtained by quantization - both aiming to smooth the empirical measure in some way in order to yield a better convergence. In this paper, we follow the approach of adapting the empirical measure by quantization as done in [8], and show that this quantized empirical measure improves the performance of conditional COT-GAN.

The process described above gives rise to *quantized conditional COT-GAN*. The main contributions of the current paper can then be summarized as follows:

- we extend the COT-GAN to a conditional framework, powered by an encoder-decoder style generator structure;
- we employ a new quantized empirical measure in the learning structure, which is a strongly consistent estimator with respect to COT;
- we show that our quantized conditional COT-GAN algorithm outperforms state-of-the-art results for video prediction.

2 Framework

We are given a dataset consisting of n i.i.d. d -dimensional sequences $(x_1^i, \dots, x_T^i)_{i=1}^n$ where $T \in \mathbb{N}$ is the number of time steps and $d \in \mathbb{N}$ is the dimensionality at each time. This is thought of as a random sample from an underlying distribution μ on $\mathbb{R}^{d \times T}$, from which we want to extract other sequences. More precisely, we want to learn the conditional distribution of (x_{k+1}, \dots, x_T) given (x_1, \dots, x_k) under μ , for any fixed $k \in \{1, \dots, T-1\}$. In the application of video prediction, an entire video contains T frames, each of which has resolution d . The first k frames of the video are taken as an input sequence, and later frames from time $k+1$ to T are the target sequence. We will use the notation $x_{s:t} = (x_s, \dots, x_t)$, for $1 \leq s \leq t \leq T$.

The conditional learning will be done via a conditional generative adversarial structure, based on a specific type of optimal transport tailored for distributions on path spaces, as introduced in the next section, in the wake of what is done in [50].

3 Optimal Transport and Causal Optimal Transport

Given two probability measures μ, ν defined on \mathbb{R}^D , $D \in \mathbb{N}$, and a cost function $c : \mathbb{R}^D \times \mathbb{R}^D \rightarrow \mathbb{R}$, the classical (Kantorovich) optimal transport of μ into ν is formulated as

$$\mathcal{W}_c(\mu, \nu) := \inf_{\pi \in \Pi(\mu, \nu)} \mathbb{E}^\pi [c(x, y)], \quad (1)$$

where $\Pi(\mu, \nu)$ is the set of probability measures on $\mathbb{R}^D \times \mathbb{R}^D$ with marginals μ, ν , which are called transport plans between μ and ν . Here $c(x, y)$ is interpreted as the cost of transporting a unit of mass from x to y . $\mathcal{W}_c(\mu, \nu)$ is thus the minimal total cost to transport the mass μ to ν . When $c(x, y)$ is a distance function between x and y (usually $\|x - y\|_p$ for some $1 \leq p < \infty$), $\mathcal{W}_c(\mu, \nu)$ is known as Wasserstein distance or Earth mover distance.

We are interested in transports between path spaces, that is, $D = d \times T$ in the above notations. Since now there is a time component intrinsic in the space \mathbb{R}^D , we are adopting a particular kind of transport which is tailored for path spaces. We denote by $x = (x_1, \dots, x_T)$ and $y = (y_1, \dots, y_T)$ the first and second half of the coordinates on $\mathbb{R}^{d \times T} \times \mathbb{R}^{d \times T}$, respectively. A probability measure π on $\mathbb{R}^{d \times T} \times \mathbb{R}^{d \times T}$ is called *causal transport plan* if it satisfies the constraint

$$\pi(dy_t | dx_{1:T}) = \pi(dy_t | dx_{1:t}) \quad \text{for all } t = 1, \dots, T-1. \quad (2)$$

Intuitively, the probability mass moved to the arrival sequence at time t only depends on the starting sequence up to time t . The set of causal plans between μ and ν is denoted by $\Pi^{\mathcal{K}}(\mu, \nu)$, and restricting the space of transport plans in (1) to such a set gives rise to the causal optimal transport problem:

$$\mathcal{W}_c^{\mathcal{K}}(\mu, \nu) := \inf_{\pi \in \Pi^{\mathcal{K}}(\mu, \nu)} \mathbb{E}^{\pi}[c(x, y)]. \quad (3)$$

COT has already found wide application in dynamic problems in stochastic calculus and mathematical finance, see e.g. [2, 1, 3, 9, 8], and first numerical results are given in [3, 50].

4 COT-GAN and CCOT-GAN

In this section we will recall the main steps that led to the COT-GAN algorithm for sequential learning in Xu et al. [50], and refer to Appendix A for the details. We then introduce a conditional version, called *conditional* COT-GAN (CCOT-GAN), suited for sequential prediction.

Solving (causal) optimal transport problems is typically computational costly for large datasets. One way to circumvent this challenge is to resort to approximations of transport problems by means of efficiently solvable auxiliary problems. Notably, Genevay et al. [20] proposed the *Sinkhorn divergence*, which allows for the use of the Sinkhorn algorithm [15]. The first observation is that (1) is the limit for $\varepsilon \rightarrow 0$ of the entropy-regularized transport problems

$$\mathcal{P}_{c,\varepsilon}(\mu, \nu) := \inf_{\pi \in \Pi(\mu, \nu)} \{\mathbb{E}^{\pi}[c(x, y)] - \varepsilon H(\pi)\}, \quad \varepsilon > 0, \quad (4)$$

where $H(\pi)$ is the Shannon entropy of π . Denoting by $\pi_{c,\varepsilon}(\mu, \nu)$ the optimizer in (4), and by $\mathcal{W}_{c,\varepsilon}(\mu, \nu) := \mathbb{E}^{\pi_{c,\varepsilon}(\mu, \nu)}[c(x, y)]$ the resulting total cost, the Sinkhorn divergence is defined as

$$\widehat{\mathcal{W}}_{c,\varepsilon}(\mu, \nu) := 2\mathcal{W}_{c,\varepsilon}(\mu, \nu) - \mathcal{W}_{c,\varepsilon}(\mu, \mu) - \mathcal{W}_{c,\varepsilon}(\nu, \nu). \quad (5)$$

Similarly, in a causal setting, we consider the entropy-regularized COT problems

$$\mathcal{P}_{c,\varepsilon}^{\mathcal{K}}(\mu, \nu) := \inf_{\pi \in \Pi^{\mathcal{K}}(\mu, \nu)} \{\mathbb{E}^{\pi}[c(x, y)] - \varepsilon H(\pi)\}, \quad \varepsilon > 0, \quad (6)$$

approximating (3). By using an equivalent characterization of causality (see Appendix A), this can be reformulated as a maximization over regularized transport problems with respect to a specific family of cost functions:

$$\mathcal{P}_{c,\varepsilon}^{\mathcal{K}}(\mu, \nu) = \sup_{c^{\mathcal{K}} \in \mathcal{C}^{\mathcal{K}}(\mu, c)} \mathcal{P}_{c^{\mathcal{K}},\varepsilon}(\mu, \nu). \quad (7)$$

The family of costs $\mathcal{C}^{\mathcal{K}}(\mu, c)$ is given by

$$\mathcal{C}^{\mathcal{K}}(\mu, c) := \left\{ c(x, y) + \sum_{j=1}^J \sum_{t=1}^{T-1} h_t^j(y) \Delta_{t+1} M^j(x) : J \in \mathbb{N}, (h^j, M^j) \in \mathcal{H}(\mu) \right\}, \quad (8)$$

where $\Delta_{t+1} M(x) := M_{t+1}(x_{1:t+1}) - M_t(x_{1:t})$ and $\mathcal{H}(\mu)$ is a set of functions depicting causality:

$$\mathcal{H}(\mu) := \{(h, M) : h = (h_t)_{t=1}^{T-1}, h_t \in \mathcal{C}_b(\mathbb{R}^{d \times t}), M = (M_t)_{t=1}^T \in \mathcal{M}(\mu), M_t \in \mathcal{C}_b(\mathbb{R}^{d \times t})\},$$

with $\mathcal{M}(\mu)$ being the set of martingales on $\mathbb{R}^{d \times T}$ w.r.t. the canonical filtration and the measure μ , and $\mathcal{C}_b(\mathbb{R}^{d \times t})$ the space of continuous, bounded functions on $\mathbb{R}^{d \times t}$. This suggests the following as a robust version of the Sinkhorn divergence from (5) that takes into account causality:

$$\sup_{c^{\mathcal{K}} \in \mathcal{C}^{\mathcal{K}}(\mu, c)} \widehat{\mathcal{W}}_{c^{\mathcal{K}},\varepsilon}(\mu, \nu).$$

This is the distance used by the discriminator in COT-GAN [50] in order to evaluate the discrepancy between real data and generated one (up to a slightly different definition of Sinkhorn divergence, see Appendix A), and it is the one we will use in the current paper for sequential prediction.

Furthermore, [50] makes the two following adjustments needed to make computations feasible. First, rather than considering the whole set of costs in (8), in (7) we optimize over a subset $\mathcal{C}^{\mathcal{K}}(\mu, c)$, by considering $\mathbf{h} := (h^j)_{j=1}^J$ and $\mathbf{M} := (M^j)_{j=1}^J$ of dimension bounded by a fixed $J \in \mathbb{N}$. Second,

instead of requiring \mathbf{M} to be a martingale, we consider all continuous bounded functions and introduce a regularization term which penalizes deviations from being a martingale. For a mini-batch of size m , $\{x_{1:T}^i\}_{i=1}^m$, sampled from the dataset, the martingale penalization for \mathbf{M} is defined as

$$p_{\mathbf{M}}(\hat{\mu}) := \frac{1}{mT} \sum_{j=1}^J \sum_{t=1}^{T-1} \left| \sum_{i=1}^m \frac{M_{t+1}^j(x_{1:t+1}^i) - M_t^j(x_{1:t}^i)}{\sqrt{\text{Var}[M^j] + \eta}} \right|,$$

where $\hat{\mu}$ is the empirical measure corresponding to the mini-batch sampled from the dataset, $\text{Var}[M]$ is the empirical variance of M over time and batch, and $\eta > 0$ is a small constant. This leads to the following objective function for COT-GAN in [50]:

$$\widehat{\mathcal{W}}_{c_{\varphi}, \varepsilon}(\hat{\mu}, \hat{\nu}_{\theta}) - \lambda p_{\mathbf{M}_{\varphi_2}}(\hat{\mu}), \quad (9)$$

where $\hat{\nu}_{\theta}$ is the empirical measure corresponding to the mini-batch produced by the generator, parameterized by θ , \mathbf{h}_{φ_1} and \mathbf{M}_{φ_2} represent the discriminator who learns the worst-case cost $c_{\varphi}^{\mathcal{K}}$, parameterized by $\varphi := (\varphi_1, \varphi_2)$, and λ is a positive constant (see Appendix A for details).

We now extend the analysis developed in [50] to a conditional framework for sequence prediction. Given the past history of a sequence up to time step k , the aim of CCOT-GAN is learning to predict the evolution from time step $k+1$ to T . As usual, the learning is done by stochastic gradient descent (SGD) on mini-batches. Given a sample $\{x_{1:T}^i\}_{i=1}^m$ from the dataset and a sample $\{z_{k+1:T}^i\}_{i=1}^m$ from a distribution ζ (noise) on some latent space \mathcal{Z} , we define the generator as a conditional model g_{θ} , parameterized by θ , which predicts the future evolution $\hat{x}_{k+1:T}^i = g_{\theta}(x_{1:k}^i, z_{k+1:T}^i)$. The prediction $\hat{x}_{k+1:T}^i$ is then concatenated with the corresponding input sequence $x_{1:k}^i$ over the time dimension in order to be compared with the training sequence $x_{1:T}^i$ by the discriminator. We denote the empirical distributions of real and concatenated data by

$$\hat{\mu} := \frac{1}{m} \sum_{i=1}^m \delta_{x_{1:T}^i}, \quad \hat{\nu}_{\theta}^c := \frac{1}{m} \sum_{i=1}^m \delta_{\text{concat}(x_{1:k}^i, \hat{x}_{k+1:T}^i)},$$

where $\hat{\nu}_{\theta}^c$ incorporates the parameterization of g_{θ} through $\{\hat{x}_{k+1:T}^i\}_{i=1}^m$. Following COT-GAN's formulation of adversarial training, we arrive at the parameterized objective function for CCOT-GAN:

$$\widehat{\mathcal{W}}_{c_{\varphi}, \varepsilon}(\hat{\mu}, \hat{\nu}_{\theta}^c) - \lambda p_{\mathbf{M}_{\varphi_2}}(\hat{\mu}). \quad (10)$$

In the implementation of CCOT-GAN, the generator g_{θ} is broken down into two components: an encoder that learns the features of input sequences $\{x_{1:k}^i\}_{i=1}^m$ and a decoder that predicts future evolutions given the features of inputs and noise $\{z_{k+1:T}^i\}_{i=1}^m$. The discriminator role is played by \mathbf{h}_{φ_1} and \mathbf{M}_{φ_2} , which are parameterized separately by two neural networks that respect temporal causality. These can take the shape of RNNs or 1D or 3D CNNs that are constrained to causal connections only, see Appendix B for details. We maximize the objective function (10) over φ to search for a robust (worst-case) distance between the two empirical measures $\hat{\mu}$ and $\hat{\nu}_{\theta}^c$, and minimize it over θ to learn a conditional model that produces plausible sequential prediction.

5 Adapted Empirical Measure and QCCOT-GAN

It was noted by Backhoff et al. [8] and Pflug and Pichler [36] that the (classical) empirical measures are not necessarily consistent estimators with respect to distances originating from transport problems where transports plans respect causality constraints. The *nested distance* [35] or *adapted Wasserstein distance* [8] is the result of an optimal transport problem where plans are required to satisfy the causality constraint (2) as well as its symmetric counterpart, when inverting the role of x and y :

$$\mathcal{AW}_c(\mu, \nu) := \inf \{ \mathbb{E}^{\pi} [c(x, y)] : \pi \in \Pi^{\mathcal{K}}(\mu, \nu), \pi' \in \Pi^{\mathcal{K}}(\nu, \mu) \}, \quad (11)$$

where $\pi'(dx, dy) = \pi(dy, dx)$.

Now, for any measure μ , and for the empirical measures $\hat{\mu}_N$ relative to a random sample of size N from it, it is known (see e.g. [19]) that

$$\mathcal{W}_c(\mu, \hat{\mu}_N) \rightarrow 0 \quad \text{as } N \rightarrow \infty,$$

whereas [8, 36] observe that this is not necessarily true when substituting the Wasserstein distance \mathcal{W}_c with the adapted Wasserstein distance \mathcal{AW}_c . This is of course undesirable, in particular thinking of the fact that the discriminator will evaluate discrepancies between real and generated measure by relying on empirical measures of the respective minibatches, see Section 4 and [50].

In [8] and [36], two different ways of adapting the empirical measure are suggested: by smoothing using a scaled kernel and by a quantization technique, respectively. We adopt the latter, as it gives optimal convergence rates when the data is high-dimensional ($d \geq 3$) in comparison to the rates provided by Wasserstein distance, see [19]. Moreover, as pointed out in [8], since the kernel-convoluted empirical measures are not discrete, they may require further quantization.

Definition 5.1. (Adapted empirical measure). Let μ be any Borel probability measure on $([0, 1]^d)^T$, and $(x^i)_{i \in \mathbb{N}}$ an i.i.d. sample from it. Set $r = (T + 1)^{-1}$ for $d = 1$ and $r = (dT)^{-1}$ for $d \geq 2$. For all $N \geq 1$, partition the cube $[0, 1]^d$ into disjoint union of N^{r^d} sub-cubes with edges of length N^{-r} . Let $\phi_N : ([0, 1]^d)^T \rightarrow ([0, 1]^d)^T$ map a sequence $x_{1:T}$ to the sequence $u_{1:T}$, where, for every t , u_t is the center of the sub-cube to which x_t belongs. Then, for any $N \in \mathbb{N}$, the *adapted empirical measure* is defined as

$$\hat{\mu}_N^A := \frac{1}{N} \sum_{i=1}^N \delta_{\phi_N(x_{1:T}^i)}. \quad (12)$$

(We will drop the index N on ϕ and $\hat{\mu}^A$ where there is no ambiguity on the size of the sample.)

A demonstration of Definition 5.1 in 2D and 3D settings is shown in Figure 1.

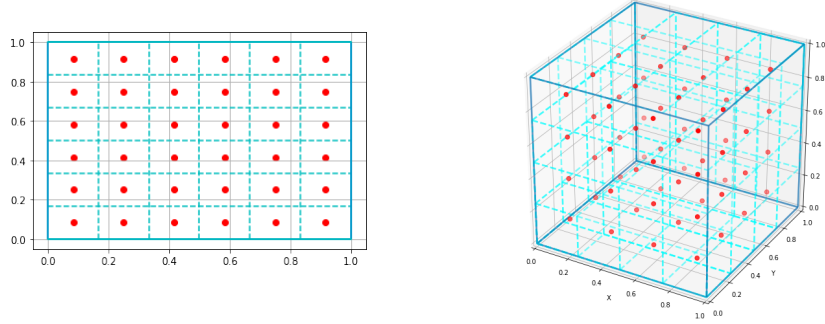


Figure 1: Illustration of adapted empirical measure, in the case $T = 1$ and $N = 500000$, for $d = 2$ (left) and $d = 3$ (right). The partition is indicated by cyan dash lines and the centroids by red dots. Any data point is mapped into the centroid of the sub-cube it belongs to.

The following theorem is an immediate consequence of results proved in [8], under appropriate conditions on the cost c and on the measure μ , see Appendix B.

Theorem 5.1. The adapted empirical measure is a strongly consistent estimator w.r.t. \mathcal{W}_c^K , that is,

$$\lim_{N \rightarrow \infty} \mathcal{W}_c^K(\mu, \hat{\mu}_N^A) = 0 \quad \text{almost surely.} \quad (13)$$

Moreover, the following estimate for the rate of convergence holds:

$$\mathbb{E}[\mathcal{W}_c^K(\mu, \hat{\mu}_N^A)] \leq C \begin{cases} N^{-\frac{1}{T+1}} & \text{for } d = 1 \\ N^{-\frac{1}{2T}} \log(N+1) & \text{for } d = 2 \\ N^{-\frac{1}{dT}} & \text{for } d \geq 3 \end{cases} \quad (14)$$

for all $N \geq 1$, where C is a positive constant that only depends on d , T , and on the Lipschitz-constant in (23).

Relying on this convergence result, we now introduce the *quantized* CCOT-GAN (QCCOT-GAN). In fact, the principle behind the concept of adapted empirical measure coincides with that of vector quantization (VQ) [23], a data compression technique widely used in computer vision and signal processing, see e.g. [30, 21, 32]. A typical VQ algorithm divides the grid into smaller blocks,

generates a discrete codebook (lookup table) using algorithms such as nearest neighbor, and maps values to discrete codes according to the codebook. The difficulty of VQ incorporated in generative models lies in finding the optimal codebook that represents the original data. Recent works [34, 37, 18] for image synthesis learn the codebook during training.

In contrast, quantization in QCCOT-GAN is theoretically justified by Theorem 5.1, and the construction of the codebook for our purpose is guided by Definition 5.1. Once a codebook is computed and stored before training starts, we can quantize the original data in real-time by

$$e_k = \phi(x_t^i) \quad \text{where} \quad k = \arg \min_j \|x_t^i - e_j\|, \quad (15)$$

and e_j represents a code (a centroid of a block in our case) in the codebook. In the context of QCCOT-GAN, we quantize the entire sequences in the mini-batches before computing the distance in (10). For a mini-batch $\{x_{1:T}^i\}_{i=1}^m$ from the training data and the concatenated sequences $\{\text{concat}(x_{1:k}^i, \hat{x}_{k+1:T}^i)\}_{i=1}^m$, we define the adapted empirical measures

$$\hat{\mu}^A := \frac{1}{m} \sum_{i=1}^m \delta_{\phi(x_{1:T}^i)}, \quad \hat{\nu}_{\theta}^{c,A} := \frac{1}{m} \sum_{i=1}^m \delta_{\phi(\text{concat}(x_{1:k}^i, \hat{x}_{k+1:T}^i))}.$$

Therefore, the objective function of QCCOT-GAN at the level of minibatches is computed on the adapted empirical measures:

$$\widehat{\mathcal{W}}_{c_{\varphi}, \varepsilon}(\hat{\mu}^A, \hat{\nu}_{\theta}^{c,A}) - \lambda p_{\mathbf{M}_{\varphi_2}}(\hat{\mu}^A). \quad (16)$$

We maximize the objective function over φ to search for a worst-case distance between the two adapted empirical measures, and minimize it over θ to learn a conditional distribution that is as close as possible to the real distribution. The algorithm is summarized in Algorithm 1. Its time complexity scales as $\mathcal{O}((J + 2d)2LTm^2)$ in each iteration. The distance $\widehat{\mathcal{W}}_{c_{\varphi}, \varepsilon}(\hat{\mu}^A, \hat{\nu}_{\theta}^{c,A})$ is approximated by the means of the Sinkhorn algorithm iteratively with a fixed number of iterations, see Appendix A.

Algorithm 1: training QCCOT-GAN by SGD

Data: $\{x_{1:T}^i\}_{i=1}^n$ (input data), ζ (probability distribution on latent space \mathcal{Z})

Parameters: θ_0, φ_0 (initialization of parameters), m (batch size), ε (regularization parameter), α (learning rate), λ (martingale penalty coefficient)

Result: θ, φ

Initialize: $\theta \leftarrow \theta_0, \varphi \leftarrow \varphi_0$

for $b = 1, 2, \dots$ **do**

Sample $\{x_{1:T}^i\}_{i=1}^m$ from real data;

Sample $\{z_{k+1:T}^i\}_{i=1}^m$ from ζ ;

Predict future sequences conditioned on inputs: $(\hat{x}_{k+1:T}^i) \leftarrow g_{\theta}(x_{1:k}^i, z_{k+1:T}^i)$;

Quantize the real and concatenated sequences: $\phi(x_{1:T}^i), \phi(\text{concat}(x_{1:k}^i, \hat{x}_{k+1:T}^i))$;

Compute $\widehat{\mathcal{W}}_{c_{\varphi}, \varepsilon}(\hat{\mu}^A, \hat{\nu}_{\theta}^{c,A})$ by the Sinkhorn algorithm;

Update discriminator parameter: $\varphi \leftarrow \varphi + \alpha \nabla_{\varphi} \left(\widehat{\mathcal{W}}_{c_{\varphi}, \varepsilon}(\hat{\mu}^A, \hat{\nu}_{\theta}^{c,A}) - \lambda p_{\mathbf{M}_{\varphi_2}}(\hat{\mu}^A) \right)$;

Sample $\{z_{k+1:T}^i\}_{i=1}^m$ from ζ ;

Predict future sequences conditioned on inputs: $(\hat{x}_{k+1:T}^i) \leftarrow g_{\theta}(x_{1:k}^i, z_{k+1:T}^i)$;

Quantize the real and concatenated sequences: $\phi(x_{1:T}^i), \phi(\text{concat}(x_{1:k}^i, \hat{x}_{k+1:T}^i))$;

Compute $\widehat{\mathcal{W}}_{c_{\varphi}, \varepsilon}(\hat{\mu}^A, \hat{\nu}_{\theta}^{c,A})$ by the Sinkhorn algorithm;

Update generator parameter: $\theta \leftarrow \theta - \alpha \nabla_{\theta} \left(\widehat{\mathcal{W}}_{c_{\varphi}, \varepsilon}(\hat{\mu}^A, \hat{\nu}_{\theta}^{c,A}) \right)$;

end

In the modern deep learning framework, learning by SGD requires all functions involved in the chain of computation to be differentiable, allowing the gradient to flow back via back-propagation. In the QCCOT-GAN algorithm, however, the argmin function in the quantization step (15) is non-differentiable. This means that the propagation of the gradient with respect to θ will not be possible.

We get around this issue by approximating the generator gradient using the straight-through estimator, see [51, 10]. When implementing QCCOT-GAN, we approximate the gradient with respect to θ by

$$\nabla_{\theta}(\widehat{\mathcal{W}}_{c_{\varphi},\varepsilon}(\widehat{\mu}^A, \widehat{\nu}_{\theta}^{c,A})) \approx \nabla_{\theta}(\widehat{\mathcal{W}}_{c_{\varphi},\varepsilon}(\widehat{\mu}, \widehat{\nu}_{\theta}^c) + sg(\widehat{\mathcal{W}}_{c_{\varphi},\varepsilon}(\widehat{\mu}^A, \widehat{\nu}_{\theta}^{c,A}) - \widehat{\mathcal{W}}_{c_{\varphi},\varepsilon}(\widehat{\mu}, \widehat{\nu}_{\theta}^c))), \quad (17)$$

where $sg(\cdot)$ is the stop gradient operation, inside which gradient tracking for any computation is disabled.

6 Related Work

Video prediction is a very active area of research. Methods relying on variational inference [13], e.g. SV2P [6], SVP-LP [16] and VTA [29], have shown promising results. The majority of adversarial models applied in this domain were trained on the original GAN objective [22] or the Wasserstein GAN objective [5]. Most efforts have been devoted to designing specific architectures that tackle the spatio-temporal dependencies separately, e.g. [47, 39, 43, 14, 31, 46], and training schemes that facilitate learning, e.g. [31, 46, 4]. Whilst some works such as TGAN [39] and VGAN [47] combined a static content generator with a motion generator, others, e.g. [43, 14], designed two discriminators to evaluate the spatial and temporal components separately. [31] explored a loss that measures gradient difference at frame level on top of an adversarial loss trained with a multi-scale architecture. As a result, better performance was achieved in comparison to a simple mean square error loss commonly used in the literature. MCnet [46] extended [31] by adopting *convolutional long short-term memory* (*ConvLSTM*) [41] in the networks. Alternatively, 3D CNN with progressively growing training scheme [28] was also shown to be successful by FutureGAN [4].

All above works depended on pixel-wise loss functions which do not take the sequential nature of video sequences into consideration. However, it may not be sufficient to rely solely on the network architecture to capture the temporal structure of data. An important development in time series synthesis and prediction is the identification of more suitable loss functions. TimeGAN [52] combined the original GAN loss with a step-wise loss that computes the distance between the conditional distributions in a supervised manner. By matching a conditional model to the real conditional probability $p(x_t|x_{1:t-1})$ at every time step, it explicitly encouraged the model to consider the temporal dependencies in the sequence. In comparison, COT-GAN [50] explored a more natural formulation for sequential generation which leads to convincing results.

In addition, quantization techniques have gained popularity in deep generative models lately. VQ-VAE [34] quantized the latent representations learned from an input image in the encoding process, and later reconstructed the image from discrete codes. A subsequent work VQ-VAE-2 [37] moved on to a multi-scale hierarchical structure which allows the mapping of discrete codes from features learned by multiple layers. In a similar spirit, VQ-GAN [18] converted learned features to discrete codes, but followed a GAN framework and employed a transformer [45] as their generator. Both VQ-VAE-2 and VQ-GAN achieved state-of-the-art results for image generation. Although working in a different application area, we emphasize the difference in how we adopt quantization with respect to those two models: first, the quantization was applied to representations in the latent space in both models, whereas we adapt the sequences in the data space. Second, the codebook in both models was learned during training, whereas it is pre-defined for QCCOT-GAN according to Definition 5.1. At last, the reason why quantization improved the results in VQ-VAE-2 and VQ-GAN is unclear. On the other hand, the improvement in convergence with the adapted empirical measures for QCCOT-GAN is supported by convergence results in causal optimal transport (Theorem 5.1).

7 Experiments

We compare QCCOT-GAN to **CCOT-GAN** without quantization as an ablation study, to **VGAN** (Vondrick et al. [47]), to **FutureGAN** (Aigner and Körner [4]), and to **SVG-LP** (Denton and Fergus [16]) as a non-adversarial baseline, on three well-established video prediction datasets. In all our experiments, the choice of cost function is $c(x, y) = \sum_t \|x_t - y_t\|_2^2$. Network architectures for generator and discriminator and training details are given in Appendix C.

KTH Human Action Dataset. The KTH Action video prediction dataset [40] contains 600 videos showing six types of human actions (humans walking, jogging, running, boxing, hand-waving, and

clapping). The length of the raw videos is up to 4 seconds with a frame rate of 25 per second and a resolution of 160×120 . We discard the first 5 frames which are often blank, and consider the next 48 frames which are further downsampled to a resolution of 64×64 . Of those, we use the first 24 frames as inputs and the last 24 as the target sequence. The dataset is divided into training set (90%) and test set (10%). Samples quantized with various levels of fineness are illustrated in Figure C.2 in Appendix C, and results from QCCOT-GAN and the chosen baselines are included in Figure 2.

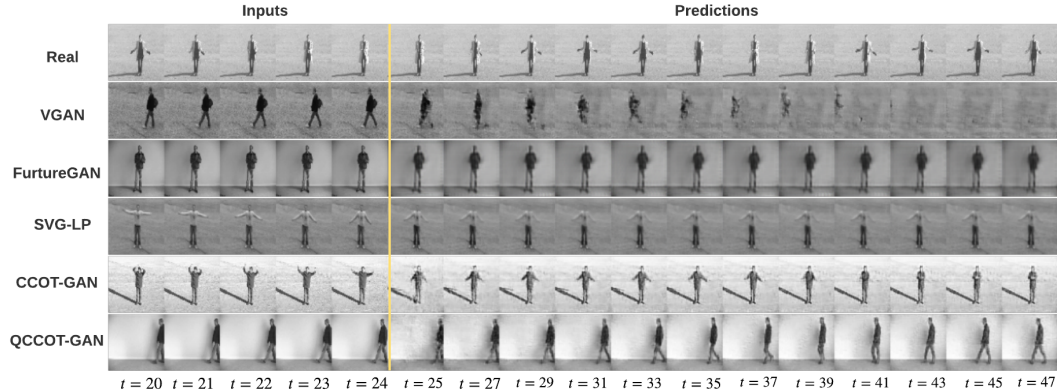


Figure 2: Selected samples trained on KTH human actions test set. Only the last 5 frames from the input sequence are shown, and the predictions are plotted every two frames. The yellow line separates the predictions from their inputs. The top line is a real sample from the test set.

Results in Figure 2 demonstrate that SVG-LP, CCOT-GAN without quantization, and QCCOT-GAN successfully captured the spatial structure in the frames to detail. However, predictions produced by SVG-LP lack of the evolution of motions, which is observed in the results from both KTH and Moving MNIST datasets (see results in Appendix C). This could be attributed to the fact that SVG-LP is conditioned on a single frame from the previous time step, which makes it impossible for the model to pick up any information about past evolution. It seems that any subtle movement of the objects is due to the randomness incorporated in the model, rather than coherent prediction learned from the data. Results for CCOT-GAN and QCCOT-GAN are visually close. We provide numerical evaluations on this dataset in Table 1.

GQN Mazes. The GQN Mazes was first introduced by [17] for training agents to learn their surroundings by moving around. The dataset contains random mazes generated by a game engine. A camera traverses one or two rooms with multiple connecting corridors in each maze. The dataset comes with a training set that contains 900 sequences and a test set with a size of 120. The original sequences have a length of 300 and resolution of 84×84 . We select the first 48 frames and again downsample them to a resolution of 64×64 . We evenly divided the training sequence of length 48 into input and target sequence. Samples quantized with various level of fineness are illustrated in Figure C.3 in Appendix C, and results from QCCOT-GAN and the chosen baseline models are provided in Figure 3.

Moving MNIST Dataset. Moving MNIST [42] contains two digits that move with velocities sampled uniformly in the range of 2 to 6 pixels per frame and bounce within the edges of each frame. The dataset has 10000 sequences, of which we use 8000 for training and the rest for testing. Each video sequence contains 20 frames with resolution 64×64 . We use the first 10 frames as input and the last 10 frames as target for prediction. Figure C.1 in Appendix C illustrates the original data and the effect of quantization with various level of fineness. All results are given in Appendix C.

Evaluation. The evaluation of sample quality in the domain of video prediction remains a challenge. We evaluate the video predictions under six metrics: Structural Similarity index [48] (SSIM, higher is better), Peak Signal-to-Noise Ratio [25] (PSNR, higher is better), the Fréchet Inception Distance [24] (FID, lower is better) and the Fréchet Video Distance [44] (FVD, lower is better) and its kernel counterparts Inception Distance and Kernel Video Distance [12] (KID and KVD, lower is better).

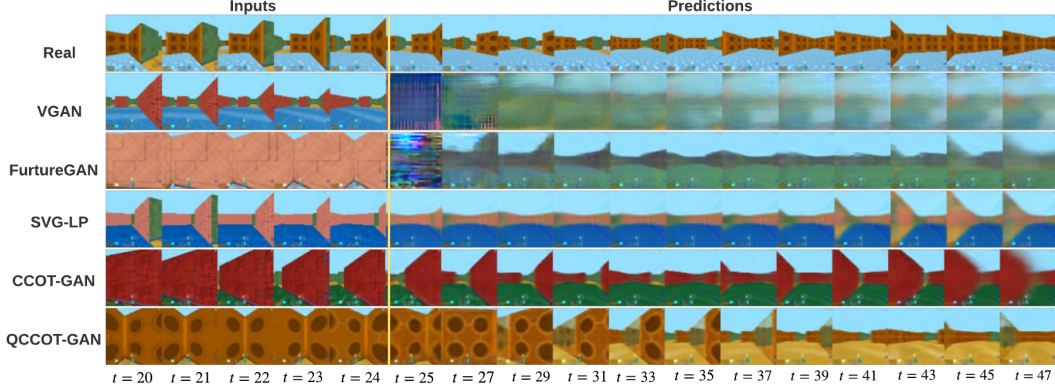


Figure 3: GQN Mazes results on the test set. Only the last 5 frames from the input sequence are shown, and the predictions are plotted every two frames. The yellow line separates the predictions from their inputs.

Table 1: Evaluations for video datasets. Lower values in the metrics indicate better sample quality.

KTH Human actions	FID	KID	FVD	KVD	SSIM	PSNR
VGAN	97.07	0.098	1092.63	0.506	0.41	15.09
FutureGAN	48.16	0.052	411.43	0.112	0.55	23.67
SVG-LP	81.19	0.062	560.80	0.197	0.57	23.87
CCOT-GAN	36.35	0.048	191.92	0.061	0.56	23.94
QCCOT-GAN	33.18	0.041	188.54	0.074	0.56	24.96
GQN Mazes						
VGAN	123.86	0.123	575.2	0.239	0.37	12.54
FutureGAN	87.70	0.116	488.3	0.245	0.41	12.53
SVG-LP	54.44	0.044	345.5	0.122	0.58	19.94
CCOT-GAN	27.8	0.039	110.3	0.033	0.65	23.50
QCCOT-GAN	21.86	0.057	77.9	0.019	0.75	26.48

All models are evaluated on the test sets with 5000 generated samples. The evaluation scores are reported in Table 1. We can see that the CCOT-GAN and QCCOT-GAN outperform the baseline models on both datasets based on FID, KID, FVD and KVD. Moreover, QCCOT-GAN achieved the highest PSNR scores across all three datasets, while SVG-LP outperforms all models in SSIM scores on the Moving MNIST (see Appendix C) and KTH datasets. VGAN and FutureGAN failed to recover the underlying distribution, while SVG-LP struggled to produce coherent movements in the prediction.

8 Discussion

In the present paper we introduce QCCOT-GAN, the first algorithm for sequence prediction that is based on recently developed modifications of optimal transport specifically tailored for path spaces. For this we build on the results by Xu et al. [50], where COT was first applied for sequential learning without prediction. Our experiments show the ability of QCCOT-GAN to not only capture the spatial structure in the frames, but also learn the complex dynamics evolving over time.

A limitation of the QCCOT-GAN algorithm is the uncertainty brought by the gradient approximation using the straight-through estimator. Differing from VQ-VAEs and VQGAN whose approximation only applies to the gradient with respect to the encoder parameters, QCCOT-GAN has to estimate that with respect to both encoder and decoder parameters. To investigate the impact of gradient approximation, future work could explore alternative methods such as the REINFORCE algorithm [10], approximation using the Gumbel-Softmax distribution [26], and stochastic perturbation [11].

We do not see any potential negative societal impacts of our work, neither coming from the methodology nor from direct potential applications. We also do not see any potential ethical concern arising from the use of the proposed approach or applications thereof.

Acknowledgments and Disclosure of Funding

This material is based upon work supported by Google Cloud.

References

- [1] B. Acciaio, J. Backhoff-Veraguas, and R. Carmona. Extended mean field control problems: stochastic maximum principle and transport perspective. *SIAM Journal on Control and Optimization*, 57(6), 2019.
- [2] B. Acciaio, J. Backhoff-Veraguas, and A. Zalashko. Causal optimal transport and its links to enlargement of filtrations and continuous-time stochastic optimization. *Stochastic Processes and their Applications*, 2019.
- [3] B. Acciaio, J. Backhoff-Veraguas, and J. Jia. Cournot-nash equilibrium and optimal transport in a dynamic setting. *arXiv preprint arXiv:2002.08786*, 2020.
- [4] S. Aigner and M. Körner. Futuregan: Anticipating the future frames of video sequences using spatio-temporal 3d convolutions in progressively growing gans. *arXiv preprint arXiv:1810.01325*, 2018.
- [5] M. Arjovsky, S. Chintala, and L. Bottou. Wasserstein generative adversarial networks. In *International conference on machine learning*, pages 214–223. PMLR, 2017.
- [6] M. Babaeizadeh, C. Finn, D. Erhan, R. H. Campbell, and S. Levine. Stochastic variational video prediction. *ICLR*, 2017.
- [7] J. Backhoff, M. Beiglbock, Y. Lin, and A. Zalashko. Causal transport in discrete time and applications. *SIAM Journal on Optimization*, 27(4):2528–2562, 2017.
- [8] J. Backhoff, D. Bartl, M. Beiglbock, and J. Wiesel. Estimating processes in adapted Wasserstein distance. *arXiv preprint arXiv:2002.07261*, 2020.
- [9] J. Backhoff-Veraguas, D. Bartl, M. Beiglbock, and M. Eder. Adapted Wasserstein distances and stability in mathematical finance. *Finance and Stochastics*, 24(3):601–632, 2020.
- [10] Y. Bengio, N. Léonard, and A. Courville. Estimating or propagating gradients through stochastic neurons for conditional computation. *arXiv preprint arXiv:1308.3432*, 2013.
- [11] Q. Berthet, M. Blondel, O. Teboul, M. Cuturi, J.-P. Vert, and F. Bach. Learning with differentiable perturbed optimizers. *arXiv preprint arXiv:2002.08676*, 2020.
- [12] M. Bińkowski, D. J. Sutherland, M. Arbel, and A. Gretton. Demystifying MMD GANs. In *ICLR*, 2018.
- [13] D. M. Blei, A. Kucukelbir, and J. D. McAuliffe. Variational inference: A review for statisticians. *Journal of the American statistical Association*, 112(518):859–877, 2017.
- [14] A. Clark, J. Donahue, and K. Simonyan. Adversarial video generation on complex datasets. *arXiv preprint arXiv:1907.06571*, 2019.
- [15] M. Cuturi. Sinkhorn distances: Lightspeed computation of optimal transport. In *NeurIPS*, 2013.
- [16] E. Denton and R. Fergus. Stochastic video generation with a learned prior. In *International Conference on Machine Learning*, pages 1174–1183. PMLR, 2018.
- [17] S. A. Eslami, D. J. Rezende, F. Besse, F. Viola, A. S. Morcos, M. Garnelo, A. Ruderman, A. A. Rusu, I. Danihelka, K. Gregor, et al. Neural scene representation and rendering. *Science*, 360(6394):1204–1210, 2018.

- [18] P. Esser, R. Rombach, and B. Ommer. Taming transformers for high-resolution image synthesis. *CVPR*, 2021.
- [19] N. Fournier and A. Guillin. On the rate of convergence in Wasserstein distance of the empirical measure. *Probability Theory and Related Fields*, 162(3):707–738, 2015.
- [20] A. Genevay, G. Peyre, and M. Cuturi. Learning generative models with sinkhorn divergences. In *AISTATS*, 2018.
- [21] A. Gersho and R. M. Gray. *Vector quantization and signal compression*, volume 159. Springer Science & Business Media, 2012.
- [22] I. J. Goodfellow, J. Pouget-Abadie, M. Mirza, B. Xu, D. Warde-Farley, S. Ozair, A. Courville, and Y. Bengio. Generative adversarial networks. *NIPS*, 2014.
- [23] R. Gray. Vector quantization. *IEEE Assp Magazine*, 1(2):4–29, 1984.
- [24] M. Heusel, H. Ramsauer, T. Unterthiner, B. Nessler, and S. Hochreiter. GANs trained by a two time-scale update rule converge to a local nash equilibrium. In *NeurIPS*, 2017.
- [25] Q. Huynh-Thu and M. Ghanbari. Scope of validity of psnr in image/video quality assessment. *Electronics letters*, 44(13):800–801, 2008.
- [26] E. Jang, S. Gu, and B. Poole. Categorical reparameterization with gumbel-softmax. *ICLR*, 2017.
- [27] N. Kalchbrenner, A. Oord, K. Simonyan, I. Danihelka, O. Vinyals, A. Graves, and K. Kavukcuoglu. Video pixel networks. In *International Conference on Machine Learning*, pages 1771–1779. PMLR, 2017.
- [28] T. Karras, T. Aila, S. Laine, and J. Lehtinen. Progressive growing of GANs for improved quality, stability, and variation. *ICLR*, 2018.
- [29] T. Kim, S. Ahn, and Y. Bengio. Variational temporal abstraction. *NeurIPS*, 2019.
- [30] J. Makhoul, S. Roucos, and H. Gish. Vector quantization in speech coding. *Proceedings of the IEEE*, 73(11):1551–1588, 1985.
- [31] M. Mathieu, C. Couprie, and Y. LeCun. Deep multi-scale video prediction beyond mean square error. *ICLR*, 2016.
- [32] N. M. Nasrabadi and R. A. King. Image coding using vector quantization: A review. *IEEE Transactions on communications*, 36(8):957–971, 1988.
- [33] J. Oh, X. Guo, H. Lee, R. Lewis, and S. Singh. Action-conditional video prediction using deep networks in atari games. *NIPS*, 2015.
- [34] A. v. d. Oord, O. Vinyals, and K. Kavukcuoglu. Neural discrete representation learning. *NeurIPS*, 2017.
- [35] G. C. Pflug and A. Pichler. A distance for multistage stochastic optimization models. *SIAM Journal on Optimization*, 22(1):1–23, 2012.
- [36] G. C. Pflug and A. Pichler. From empirical observations to tree models for stochastic optimization: convergence properties. *SIAM Journal on Optimization*, 26(3):1715–1740, 2016.
- [37] A. Razavi, A. v. d. Oord, and O. Vinyals. Generating diverse high-fidelity images with VQ-VAE-2. *NeurIPS*, 2019.
- [38] S. Reed, A. Oord, N. Kalchbrenner, S. G. Colmenarejo, Z. Wang, Y. Chen, D. Belov, and N. Freitas. Parallel multiscale autoregressive density estimation. In *International Conference on Machine Learning*, pages 2912–2921. PMLR, 2017.
- [39] M. Saito, E. Matsumoto, and S. Saito. Temporal generative adversarial nets with singular value clipping. In *ICCV*, 2017.

- [40] C. Schuldt, I. Laptev, and B. Caputo. Recognizing human actions: a local svm approach. In *Proceedings of the 17th International Conference on Pattern Recognition, 2004. ICPR 2004.*, volume 3, pages 32–36. IEEE, 2004.
- [41] X. Shi, Z. Chen, H. Wang, D.-Y. Yeung, W.-K. Wong, and W.-c. Woo. Convolutional LSTM network: A machine learning approach for precipitation nowcasting. *arXiv preprint arXiv:1506.04214*, 2015.
- [42] N. Srivastava, E. Mansimov, and R. Salakhudinov. Unsupervised learning of video representations using LSTMs. In *International conference on machine learning*, pages 843–852. PMLR, 2015.
- [43] S. Tulyakov, M.-Y. Liu, X. Yang, and J. Kautz. Mocogan: Decomposing motion and content for video generation. In *CVPR*, 2018.
- [44] T. Unterthiner, S. van Steenkiste, K. Kurach, R. Marinier, M. Michalski, and S. Gelly. Towards accurate generative models of video: A new metric & challenges. *arXiv preprint arXiv:1812.01717*, 2018.
- [45] A. Vaswani, N. Shazeer, N. Parmar, J. Uszkoreit, L. Jones, A. N. Gomez, L. Kaiser, and I. Polosukhin. Attention is all you need. *NeurIPS*, 2017.
- [46] R. Villegas, J. Yang, S. Hong, X. Lin, and H. Lee. Decomposing motion and content for natural video sequence prediction. *ICLR*, 2017.
- [47] C. Vondrick, H. Pirsiavash, and A. Torralba. Generating videos with scene dynamics. In *NeurIPS*, 2016.
- [48] Z. Wang, A. C. Bovik, H. R. Sheikh, and E. P. Simoncelli. Image quality assessment: from error visibility to structural similarity. *IEEE transactions on image processing*, 13(4):600–612, 2004.
- [49] D. Weissenborn, O. Täckström, and J. Uszkoreit. Scaling autoregressive video models. *ICLR*, 2020.
- [50] T. Xu, L. K. Wenliang, M. Munn, and B. Acciaio. COT-GAN: Generating Sequential Data via Causal Optimal Transport. In *NeurIPS*, 2020.
- [51] P. Yin, J. Lyu, S. Zhang, S. Osher, Y. Qi, and J. Xin. Understanding straight-through estimator in training activation quantized neural nets. *ICLR*, 2019.
- [52] J. Yoon, D. Jarrett, and M. van der Schaar. Time-series generative adversarial networks. In *NeurIPS*. 2019.

Quantized Conditional COT-GAN for Video Prediction:

Supplementary material

A Details on regularized Causal Optimal Transport

A.1 Sinkhorn algorithm

The entropy-regularized transport problems (4) is obtained by considering an entropic constraint. For transport plans with marginals μ supported on a finite set $\{x^i\}_i$ and ν on a finite set $\{y^j\}_j$, any $\pi \in \Pi(\mu, \nu)$ is also discrete with support on the set of all possible pairs $\{(x^i, y^j)\}_{i,j}$. Denoting $\pi_{ij} = \pi(x^i, y^j)$, the Shannon entropy of π is given by $H(\pi) := -\sum_{i,j} \pi_{ij} \log(\pi_{ij})$. A transport plan in the discrete case can be considered as a table identified with a joint distribution. The intuition of imposing such a regularization is to restrict the search of couplings to tables with sufficient smoothness in order to improve efficiency.

When the measures are discrete, such a regularized optimal transport problem becomes easily solvable by using the Sinkhorn algorithm for a given number of iterations, say L , in order to approximate a solution to the Sinkhorn divergence (5), see [20] for detail. Generally speaking, the stronger the regularization is (that is, the bigger the parameter ϵ is), the fewer number of iterations L is needed in order to yield a good approximation.

A.2 Sinkhorn divergence at the level of mini-batches

To correct the fact that $\mathcal{W}_{c,\epsilon}(\alpha, \alpha) \neq 0$, the Sinkhorn divergence proposed by Genevay et al. [20] at the mini-batch level is written as

$$\widehat{\mathcal{W}}_{c,\epsilon}(\widehat{\mu}, \widehat{\nu}_\theta) := \mathcal{W}_{c,\epsilon}(\widehat{\mu}, \widehat{\nu}_\theta) - \mathcal{W}_{c,\epsilon}(\widehat{\mu}, \widehat{\mu}) - \mathcal{W}_{c,\epsilon}(\widehat{\nu}_\theta, \widehat{\nu}_\theta), \quad (18)$$

where the empirical measures $\widehat{\mu}$ and $\widehat{\nu}_\theta$ correspond to mini-batch sampled from the dataset and that produced by the model, respectively.

This is an attempt to correct the bias introduced by the entropic regularization via eliminating the differences brought by the variations in both mini-batches of the real and generated samples. However, an experiment in [50] shows that the above formulation (18) failed to reduce the bias and recover the optimizer set up as a known quantity. Therefore, the authors propose the mixed Sinkhorn divergence,

$$\widehat{\mathcal{W}}_{c,\epsilon}^{\text{mix}}(\widehat{\mu}, \widehat{\mu}', \widehat{\nu}_\theta, \widehat{\nu}'_\theta) := \mathcal{W}_{c,\epsilon}(\widehat{\mu}, \widehat{\nu}_\theta) + \mathcal{W}_{c,\epsilon}(\widehat{\mu}', \widehat{\nu}'_\theta) - \mathcal{W}_{c,\epsilon}(\widehat{\mu}, \widehat{\mu}') - \mathcal{W}_{c,\epsilon}(\widehat{\nu}_\theta, \widehat{\nu}'_\theta),$$

where $\widehat{\mu}$ and $\widehat{\mu}'$ correspond to different mini-batches from the dataset, and $\widehat{\nu}$ and $\widehat{\nu}'$ from generated samples. Instead of considering the variations within a batch, the mixed Sinkhorn divergence reduces the bias by excluding the variations in different mini-batches from the same underlying distribution.

Alternative mini-batch Sinkhorn divergences are also investigated in [50], for example,

$$\begin{aligned} \widehat{\mathcal{W}}_{c,\epsilon}^6(\widehat{\mu}, \widehat{\mu}', \widehat{\nu}_\theta, \widehat{\nu}'_\theta) &= \mathcal{W}_{c,\epsilon}(\widehat{\mu}, \widehat{\nu}_\theta) + \mathcal{W}_{c,\epsilon}(\widehat{\mu}', \widehat{\nu}_\theta) + \mathcal{W}_{c,\epsilon}(\widehat{\mu}, \widehat{\nu}'_\theta) \\ &\quad + \mathcal{W}_{c,\epsilon}(\widehat{\mu}', \widehat{\nu}'_\theta) - 2\mathcal{W}_{c,\epsilon}(\widehat{\mu}', \widehat{\mu}') - 2\mathcal{W}_{c,\epsilon}(\widehat{\nu}, \widehat{\nu}'_\theta). \end{aligned}$$

In sequential generation (without conditioning), the results in [50] suggest that $\widehat{\mathcal{W}}_{c,\epsilon}^{\text{mix}}$ and $\widehat{\mathcal{W}}_{c,\epsilon}^6$ outperform all other formulations of mini-batch Sinkhorn divergence in both the low-dimensional experiments and video generation. Although $\widehat{\mathcal{W}}_{c,\epsilon}^{\text{mix}}$ and $\widehat{\mathcal{W}}_{c,\epsilon}^6$ produce equally good results, $\widehat{\mathcal{W}}_{c,\epsilon}^6$ is computationally more expensive because it requires two more terms in the computation.

In the case of sequential prediction, $\widehat{\mathcal{W}}_{c,\epsilon}(\widehat{\mu}, \widehat{\nu}_\theta)$ is employed in the QCCCOT-GAN algorithm. Recall that $\widehat{\nu}_\theta$ denotes the empirical measure of the concatenated sequences which share the input sequences with the real sequences up to time step k . As a result, it is not sensible to account for the variations in two batches from the same distribution that do not coincide before time step k as $\widehat{\mu}$ and $\widehat{\nu}_\theta$ do. Hence, we consider $\widehat{\mathcal{W}}_{c,\epsilon}(\widehat{\mu}, \widehat{\nu}_\theta)$ a more appropriate objective function for prediction under the setting of QCCCOT-GAN.

A.3 An equivalent characterization of causality

The expression (7) obtained in Section 4 relies on the following characterization of causality, proved in [7]: a transport plan $\pi \in \Pi(\mu, \nu)$ is causal if and only if

$$\mathbb{E}^\pi \left[\sum_{t=1}^{T-1} h_t(y) \Delta_{t+1} M(x) \right] = 0 \quad \text{for all } (h, M) \in \mathcal{H}(\mu). \quad (19)$$

With an abuse of notation we write $h_t(y)$, $M_t(x)$, $\Delta_{t+1} M(x)$ rather than $h_t(y_{1:t})$, $M_t(x_{1:t})$, $\Delta_{t+1} M(x_{1:t+1})$.

A.4 Details about COT-GAN

Adopting the mixed Sinkhorn divergence, COT-GAN is trained on the following objective function

$$\widehat{\mathcal{W}}_{c,\epsilon}^{\text{mix},L}(\widehat{\mu}, \widehat{\mu}', \widehat{\nu}_\theta, \widehat{\nu}_\theta') - \lambda p_{\mathbf{M}_{\varphi_2}}(\widehat{\mu}), \quad (20)$$

where L indicates the number of iterations required for approaching a solution to the mixed Sinkhorn divergence.

To formulate an adversarial training algorithm for implicit generative models, COT-GAN approximates the set of functions (8) by truncating the sums at a fixed J , and parameterizes $\mathbf{h}_{\varphi_1} := (h_{\varphi_1}^j)_{j=1}^J$ and $\mathbf{M}_{\varphi_2} := (M_{\varphi_2}^j)_{j=1}^J$ as two separate neural networks, and let $\varphi := (\varphi_1, \varphi_2)$. To capture the characteristics of those processes, the choices of network architecture are restricted to those with causal connections only. The mixed Sinkhorn divergence is then calculated with respect to a parameterized cost function

$$c_\varphi^{\mathcal{K}}(x, y) := c(x, y) + \sum_{j=1}^J \sum_{t=1}^{T-1} h_{\varphi_1,t}^j(y) \Delta_{t+1} M_{\varphi_2}^j(x), \quad (21)$$

where the cost function is chosen to be $c(x, y) = \|x - y\|_2^2$ in COT-GAN.

While the generator $g_\theta : \mathcal{Z} \rightarrow \mathcal{X}$ is incorporated in $\widehat{\nu}_\theta$, the discriminator role in COT-GAN is played by \mathbf{h}_{φ_1} and \mathbf{M}_{φ_2} . COT-GAN learns a robust (worst-case) distance between the real data distribution and the generated distribution by maximizing the objective (20) over φ , and a strong generator to fool the discriminator by minimizing the mixed divergence over θ .

B Specifics on QCCOT-GAN

B.1 Adapted empirical measure

The adapted empirical measure adopted for QCOT-GAN has been introduced by Backhoff et al. [8] as a strongly consistent estimator with respect to a specific \mathcal{AW} -distance. We recall here their main results.

For a probability measure μ on $\mathbb{R}^{d \times T}$ and $1 \leq t \leq T - 1$, we denote by μ_1 the first marginal of μ and by μ_{x_1, \dots, x_t} the disintegration of μ , that is

$$\mu_1(\cdot) = \text{Prob}(X_1 \in \cdot), \quad \mu_{x_1, \dots, x_t}(\cdot) = \text{Prob}(X_{t+1} \in \cdot | X_1 = x_1, \dots, X_t = x_t),$$

for all $(x_1, \dots, x_t) \in \mathbb{R}^{d \times t}$, where X is a process with law μ .

Let us denote by \mathcal{AW}_1 the adapted Wasserstein distance relative to the cost function $c^1 : \mathbb{R}^{d \times T} \times \mathbb{R}^{d \times T} \rightarrow \mathbb{R}$ given by $c^1(x, y) := \sum_{t=1}^T \|x_t - y_t\|_1$. Then Theorems 1.3 and 1.5 in [8] read as

Theorem B.1. The adapted empirical measure $\widehat{\mu}_N^A$ satisfies

$$\lim_{N \rightarrow \infty} \mathcal{AW}_1(\mu, \widehat{\mu}_N^A) = 0 \quad \text{almost surely.} \quad (22)$$

Moreover, if μ has Lipschitz kernels in the sense that for every $1 \leq t \leq T - 1$ the mapping

$$(x_1, \dots, x_t) \mapsto \mu_{x_1, \dots, x_t} \quad \text{is Lipschitz continuous} \quad (23)$$

w.r.t. the classical Wasserstein distance, then there is a constant $C > 0$ (only dependent on d, T , and on the Lipschitz-constant) such that

$$\mathbb{E}[\mathcal{AW}_1(\mu, \hat{\mu}_N^A)] \leq C \begin{cases} N^{-\frac{1}{T+1}} & \text{for } d = 1 \\ N^{-\frac{1}{2T}} \log(N+1) & \text{for } d = 2 \\ N^{-\frac{1}{dT}} & \text{for } d \geq 3 \end{cases} \quad (24)$$

for all $N \geq 1$.

In order to deduce the results on \mathcal{W}_c^K stated in Section 5, notice that

$$\mathcal{W}_c^K(\mu, \nu) \leq \mathcal{AW}_c(\mu, \nu) \quad (25)$$

for any probability measures μ, ν and any cost function c , given that the set of transports over which minimization is done for causal optimal transport is bigger than that for \mathcal{AW} -distance, cf. (3) and (11).

Proof of Theorem 5.1. With cost function c^1 , it immediately follows from Theorem B.1 and (25). \square

The proof of Theorem B.1 relies on a dynamic programming representation for the value of the bicausal optimal transport problem, see [7]. This can be generalized from c^1 to cost functions c that are separable in the sense that they can be written as

$$c(x, y) = \sum_{t=1}^T c_t(x_t, y_t),$$

for some functions c_t on $\mathbb{R}^d \times \mathbb{R}^d$. For example, under the following modulus of continuity assumption on μ w.r.t. c (generalizing the Liptchitz assumption above)

$$\mathcal{W}_{c_{t+1}}(\mu_{x_1, \dots, x_t}, \mu_{y_1, \dots, y_t}) \leq L \sum_{s=1}^t c_s(x_s, y_s),$$

we have that for $T = 2$ there is $C > 0$ such that

$$\mathcal{AW}_c(\mu, \nu) = \inf_{\gamma \in \Pi(\mu_1, \nu_1)} \int c_1(x_1, y_1) + \mathcal{W}_{c_2}(\mu_{x_1}, \nu_{y_1}) \gamma(dx_1, dy_1) \quad (26)$$

$$\leq C \mathcal{W}_{c_1}(\mu_1, \nu_1) + C \int \mathcal{W}_{c_2}(\mu_{y_1}, \nu_{y_1}) \nu(dy), \quad (27)$$

and for any $T \in \mathbb{N}$ there is $C > 0$ such that

$$\mathcal{AW}_c(\mu, \nu) \leq C \mathcal{W}_{c_1}(\mu_1, \nu_1) + C \sum_{t=1}^{T-1} \int \mathcal{W}_{c_{t+1}}(\mu_{y_1, \dots, y_t}, \nu_{y_1, \dots, y_t}) \nu(dy).$$

Based on these estimates, and following the lines of the proofs of Theorems 1.3 and 1.5 in [8], one arrives at different rates of convergence for $\mathbb{E}[\mathcal{AW}_c(\mu, \hat{\mu}_N^A)]$ that depend on the cost function c .

B.2 Codebook and quantization

In this section, we detail the computation of the codebook used in QCCOT-GAN, see Definition 5.1. Given N sequences with dimension d and length T , the number of sub-cubes is N^{rd} , which is not necessarily an integer for $r = (T+1)^{-1}$ when $d = 1$ and $r = (dT)^{-1}$ when $d \geq 2$. In the implementation, we first compute the number of partitions along one dimension by taking the ceiling function of the length of the entire cube (length of 1 in this case) divided by the length of the sub-cubes N^{-r} , that is,

$$N^p = \lceil \frac{1}{N^{-r}} \rceil, \quad (28)$$

where $\lceil \cdot \rceil$ indicates the ceiling function.

Next, we find the end points of N^p partitions, and then the mid-points of them which we store in the codebook as discrete codes. Every dimension should have the same codes as the length of the

Table 2: Encoder and decoder architecture.

Encoder Configuration	
Input	input with shape with $T \times 4 \times 4 \times 256$
1	convLSTM2D(N32, K5, S2, P=SAME), BN
2	convLSTM2D(N64, K5, S2, P=SAME), BN
3	convLSTM2D(N128, K5, S2, P=SAME), BN
4	convLSTM2D(N256, K5, S2, P=SAME), BN
5	output features f^{enc} with shape $T \times 4 \times 4 \times 256$
Decoder Configuration	
Input	$z \sim \mathcal{N}(\mathbf{0}, \mathbf{I}), f^{\text{enc}}$
0	convLSTM2D(N256, K5, S1, P=SAME), BN
1	DCONV(N256, K2, S2, P=SAME), BN
2	convLSTM2D(N128, K9, S1, P=SAME), BN
3	DCONV(N128, K4, S2, P=SAME), BN
4	convLSTM2D(N64, K9, S1, P=SAME), BN
5	DCONV(N64, K6, S2, P=SAME), BN
6	convLSTM2D(N32, K9, S1, P=SAME), BN
7	DCONV(N3, K6, S2, P=SAME)

sub-cubes remains the same along every dimension. This largely simplifies the computation of the codebook used in QCCOT-GAN. Once the codebook is computed, we can quantize the data by mapping each value to the nearest discrete code, as suggested in (15). Parallel lookups available in the modern deep learning frameworks stream the quantization step very well on GPU architectures, and therefore lower the computational cost. For data with extremely high dimensionality and long length, we would recommend to quantize the real dataset and store the discrete codes prior to training. However, in our experiments, the computation cost of quantization did not cause concerns. We therefore applied quantization to both real and generated batches in real-time computing.

Finally we point out a situation where quantization may cause issues. When a given dataset has a wide spread of values, quantization according to Definition 5.1 may emphasize the key messages and ignore details in the data, see examples in Figures 5 and 6. On the other hand, if the data is binary or the spread of values is extremely narrow, such quantization may weaken, or even destroy, the pattern exhibited in the data, see an example in Figure 4.

C Experiment details

C.1 Network architectures and training details

All three databases in the experiments share the same GAN architectures. The generator is split into an encoder and a decoder, supported by convolutional LSTM (convLSTM). The encoder learns both the spatial and temporal features of the input sequences, whereas the decoder predicts the future evolution conditioned on the learned features and a latent variable.

The features from the last encoding layer has a shape of 4×4 (height \times width) per time step. A latent variable z is sampled from a multivariate standard normal distribution with the same shape as the features (same number of channels too depending on the model size). We then concatenate the features and latent variables over the channel dimension as input for the decoder. The encoder and decoder structures are detailed in Table 2. As the discriminator, the process \mathbf{h} and \mathbf{M} are parameterized with two separate networks that share the same structure, shown in Table 3. In all tables, we use DCONV to represent a de-convolutional (convolutional transpose) layer. The layers may have N filter size, K kernel size, S strides and P padding option. We adopt batch-normalization layers and the LeakyReLU activation function. All hyperparameter setting are the same for all three datasets except that the filter size is halved for the Moving MNIST dataset. The KTH, GQN Mazes and moving MNIST datasets have a fixed length of 48, 48, and 20, respectively. The maximum filter size in the convLSTM layer in the generator is 256 for KTH and GQN Mazes datasets and 128 for moving MNIST. Although convLSTM is computationally costly, our model size is much smaller than the baseline models which often scale up to a filter size of 1024. For this reason, the computation time for the QCCOT-GAN experiments is similar to that for the baseline models.

Table 3: Discriminator architecture.

Discriminator	Configuration
Input	64x64x3
0	CONV(N32, K5, S2, P=SAME), BN, LeakyReLU
1	CONV(N64, K5, S2, P=SAME), BN, LeakyReLU
2	CONV(N128, K5, S2, P=SAME), BN, LeakyReLU
3	reshape to 3D array of shape (m, T, -1) as input for LSTM
4	LSTM(state size = 128), BN
5	LSTM(state size = 64)
6	LSTM(state size = 32)

To guarantee convergence, we choose the lowest possible number of partitions N^p for quantization without losing too much information. We set $N^p = 3$ for the Moving MNIST and KTH datasets and $N^p = 2$ for the GQN mazes. During training, we apply exponential decay to the learning rate by $\eta_t = \eta_0 r^{s/c}$ where η_0 is the initial learning rate, r is decay rate, s is the current number of training steps and c is the decaying frequency. In our experiments, the initial learning rate is 0.0005, decay rate 0.985, decaying frequency 10000, and batch size $m = 8$ for all datasets. We have $\lambda = 1.0$, $\varepsilon = 0.8$ and the Sinkhorn iterations $L = 100$ in all experiments. We train QCCOT-GAN on a single NVIDIA Tesla V100 GPU on Google Cloud Platform. Each iteration takes roughly 0.4 second for the moving MNIST dataset, and 1.3 seconds for the KTH and GQN Mazes datasets. Each experiment is run for around 100000 iterations. For the Moving MNIST dataset, we use an autoregressive structure, which predicts one future step conditioned on the most recent past 10 steps, to boost performance, whilst multi-step prediction (predicts 24 frames conditioned on previous 24 frames) is done for KTH and GQN Mazes. This is because we observe that the model tends to forget the static features in later steps of prediction on the test set of Moving MNIST. A possible explanation for this is that the quantization step in QCCOT-GAN weakens the features for this type of data. At last, we also adopt early stopping in order to avoid overfitting-caused poor results on the test sets in all experiments.

C.2 Quantization with multiple level of fineness

We provide examples to illustrate the effect of quantization on the original Moving MNIST, KTH and GQN Mazes data for different levels of fineness depending on the number of sub-cubes N^p .

Figure 4: Moving MNIST. From top to bottom: original, quantized sequences for $N^p = 5, 3$, and 2.

C.3 Results on Moving MNIST

Unfortunately, the same evaluation metrics (FID, FVD, KID, and KVD) used for KTH human action and the GQN Mazes results become inappropriate when evaluating the Moving MNIST results. This is because those metrics involve extracting features from the real and generated samples using 2D or 3D convolutional layers which are pre-trained on benchmark datasets that consist of colorful images

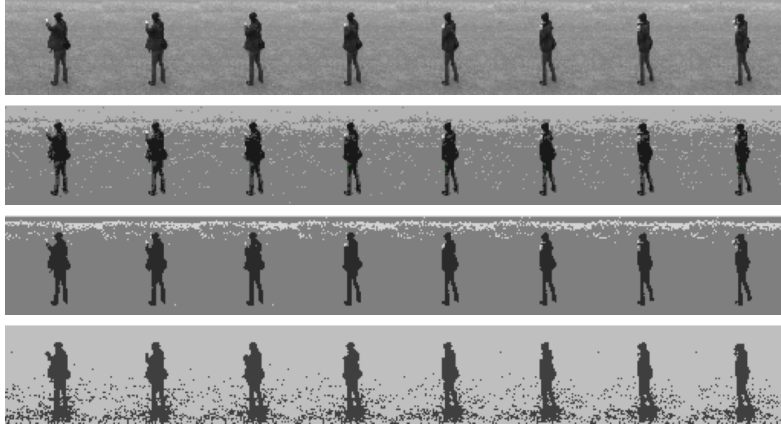


Figure 5: KTH. From top to bottom: original, quantized sequences for $N^p = 5, 3$, and 2.

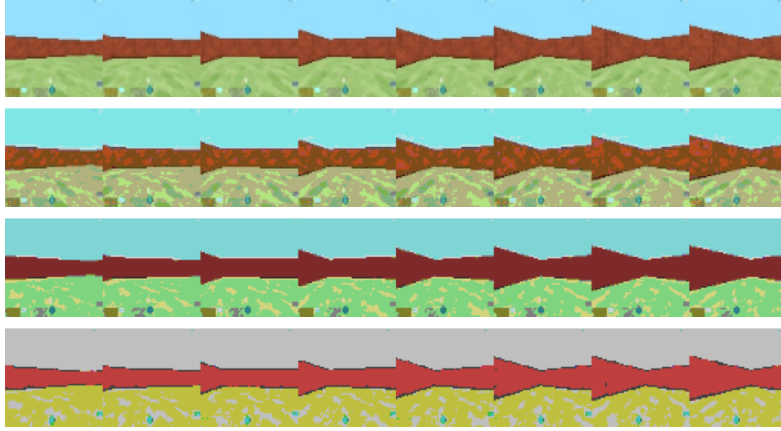


Figure 6: GQN mazes. From top to bottom: original, quantized sequences for $N^p = 5, 3$, and 2.

	Inputs					Predictions														
Real	0	0	0	0	0	0	0	0	0	0	0	0	0	0	0	0	0	0	0	0
VGAN	0	0	0	0	0	0	0	0	0	0	0	0	0	0	0	0	0	0	0	0
FurtureGAN	0	0	0	0	0	0	0	0	0	0	0	0	0	0	0	0	0	0	0	0
SVG-LP	5	5	5	5	5	5	5	5	5	5	5	5	5	5	5	5	5	5	5	5
CCOT-GAN	0	0	0	0	0	0	0	0	0	0	0	0	0	0	0	0	0	0	0	0
QCCOT-GAN	4	4	4	4	4	4	4	4	4	4	4	4	4	4	4	4	4	4	4	4
	$t=6$	$t=7$	$t=8$	$t=9$	$t=10$	$t=11$	$t=12$	$t=13$	$t=14$	$t=15$	$t=16$	$t=17$	$t=18$	$t=19$	$t=20$					

Figure 7: Moving MNIST results on test set.

or videos with RGB channels. However, the Moving MNIST dataset contains black and white (or gray) video sequences with a single channel. As a result, the features extracted from the pre-trained layers may not lead to a meaningful evaluation. Instead, we measure the quality of the Moving MNIST predictions using two alternative metrics: Structural Similarity index [48] (SSIM, higher is

Table 4: Evaluations for Moving MNIST datasets. Higher values in SSIM and PSNR indicate better sample quality.

	Moving MNIST	
	SSIM	PSNR
VGAN	0.40	12.18
FutureGAN	0.49	14.59
SVG-LP	0.75	16.10
CCOT-GAN	0.40	12.17
QCCOT-GAN	0.70	16.14

better) and Peak Signal-to-Noise Ratio [25] (PSNR, higher is better). Results on the Moving MNIST dataset are presented in Figure 7 and Table 4.